A PROBABILISTIC SEGMENTATION METHOD FOR IVUS IMAGES

Gerardo Mendizabal-Ruiz, Mariano Rivera and Ioannis A. Kakadiaris

Comunicación Técnica No I-07-17/13-12-2007
(CC/CIMAT)

A probabilistic segmentation method for IVUS images

Gerardo Mendizabal-Ruiz
CIMAT
egerardo@cimat.mx

Mariano Rivera
CIMAT
mrivera@cimat.mx

Ioannis A. Kakadiaris
University of Houston
www.cbl.uh.edu

Abstract

Intravascular ultrasound (IVUS) is a catheter-based medical imaging technique that produces cross-sectional images of blood vessels and is particularly useful for studying atherosclerosis. In this paper, we present a probabilistic approach for the semi-automatic segmentation of the luminal border on IVUS images. Specifically, we parameterize the lumen contour using a sum of Gaussian functions that are deformed by the minimization of a cost function formulated using a probabilistic approach. For the optimization of the cost function, we introduce a novel method that linearly combines the descent directions of the steepest descent and BFGS optimization methods within a trust region that improves convergence. Results of our proposed method on 20 MHz IVUS images are presented and discussed in order to demonstrate the effectiveness of our approach.

1. Introduction

Complications attributed to cardiovascular disease (CVD) are currently the main cause of death worldwide. It is known that the majority of adverse CVD-related events are due to coronary artery disease: a condition in which fatty lesions called plaques are formed on the walls of those vessels which nourish the heart with blood.

Intravascular ultrasound (IVUS) is an invasive imaging technique capable of providing high-resolution, cross-sectional images of the interior of human blood vessels in real time; this allows the collection of morphological information of the vessel, and by consequence of the plaque. Segmentation of IVUS images refers to the delineation of the lumen/intima and media/adventita borders. This process is necessary for assessing the vessel and plaque characteristics.

Given that IVUS sequences may be hundreds to thousands of frames long, the manual segmentation of a complete sequence is prohibitively time-consuming. Thus, an automatic segmentation method for IVUS images is needed.

In this paper we present a method for semi-automatic segmentation of the lumen contour on IVUS images and video sequences. Our contributions are: 1) a probabilistic approach to the segmentation problem that introduces a new parameterization of the lumen contour using a sum of Gaussian functions that is deformed by the minimization of a cost function formulated using Markov-random field models with a Bayesian approach inspired by the segmentation method proposed by Rivera *et al* [9]; 2) a novel minimization method that linearly combines the descent directions of the *steepest descent* and *BFGS* optimization methods within a trust region that stabilizes the convergence; and 3) a multi-scale approach that increases considerably the speed of convergence.

The rest of the paper is organized as follow: Section 2 presents previous work in IVUS segmentation, Section 3 presents the methods for our segmentation method, Section 4 presents the results obtained with our method, and Section 5 presents our conclusions.

2. Previous work

A number of segmentation techniques have been developed for IVUS data analysis. A major portion was based on local properties of image pixels, namely gradient based active surfaces [5] and pixel intensity combined with gradient active contours [6]. Graph search was also investigated using local pixel features and gradient associated to line patterns correlation [14] [13].

Another set of works was based on global region information. Texture-based morphological processing was considered [7]. Gray level variances were then used for the optimization of a maximum *a posteriori* (MAP) estimator modeling ultrasound speckle and contour geometry [4].

Recently, most reported successful approaches are based on contour detection using a minimization of a cost function of the boundary contours or deformable models. On the first approaches, Sonka *et al* [10] implemented a knowledge-based graph searching method incorporating *a priori* knowledge of coronary artery anatomy and a selected region of interest prior to the automatic border detection. Brusseau *et al* [2] exploited an automatic method for detecting the luminal border based on an active contour that evolves until it optimally separates regions with different statistical properties.

Recently, Unal *et al* [12] introduced a shape-driven approach to segmentation of the arterial wall from IVUS images in the polar B-mode representation. The contours or shapes in a training dataset are first aligned to build an average shape and then eigenshapes are obtained (shape space) through principal component analysis (PCA) to describe the variations from the mean shape. Then, any contour can be described as a weighted linear combination of the first k eigenshapes. To obtain the weight for each contour, the minimum of a non-parametric energy is computed by solving an ordinary differential equation.

Previous IVUS image segmentation methods are almost always hampered by noise and artifacts presented on the IVUS images. Although active shape models have been shown to be robust to this problem, a training phase is required to provide the statistical knowledge that allows for segmentation of new images. However, having a training set that is sufficiently representative of all possible IVUS images is a difficult task due to the different shapes that the vessels can take and the variability of the IVUS catheters. In these cases an IVUS image that is dissimilar in shape to those on the training set will be very difficult to segment with this method.

In summary, previous techniques were not able to solve the segmentation problem efficiently due to IVUS artifacts, and those that have shown better performance require a prior training phase. Next, we present a probabilistic approach for segmentation of the lumininal border of IVUS images that does not require training and that is robust to artifacts.

3. Methods

Similarly to [12], we employ a B-mode polar IVUS image representation. This choice makes the computations much simpler due to the 1D appearance of the interfaces to be detected (Fig. 1). Thus, in the IVUS image domain $\Omega \epsilon \Re^2$, we define the grey-level pixel intensity as $I(x)$ for a pixel with coordinates $x = (\theta, r)$ where $(\{\theta, r\} \epsilon \Omega)$ are the angle and radius of the IVUS image (Fig. 2), respectively. In this domain, we parameterize the lumen contour as a function $f(\theta, C)$ that depends on the angle and the parameters C.

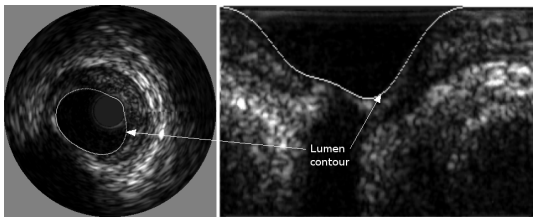

Figure 1. Lumen contour in Cartesian (left) and polar (right) B-mode representations

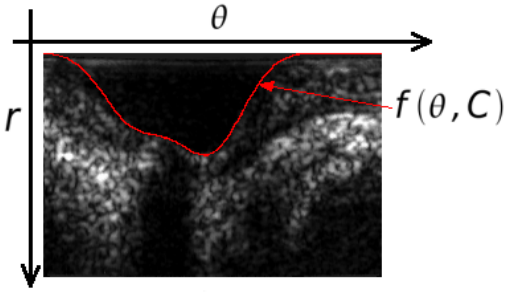

Figure 2. Contour function on rectangular image domain.

Since we want the lumen contour to be a smooth periodic curve, we propose modeling the lumen contour as a Gaussian sum. Then, the smoothness can be controlled by the number of Gaussians and their standard deviations. To reduce the computational cost, we have decided to fix the number of Gaussians N and use the same standard deviation σ for all the Gaussians. Then, the lumen contour $f(\theta, C)$ with parameters $C = \{C_0, C_1, ..., C_N\}$ for an IVUS image with width w is

given by:

$$f(\theta, C) = C_0^2 + \sum_{i=1}^{N} C_i^2 \exp(-\frac{1}{2\sigma^2}(\theta - \mu_i)^2) + \sum_{i=1}^{N} C_i^2 \exp(-\frac{1}{2\sigma^2}(\theta + (w-1) - \mu_i)^2) + \sum_{i=1}^{N} C_i^2 \exp(-\frac{1}{2\sigma^2}(\theta - (w-1) - \mu_i)^2) \quad (1)$$

where C_0 is an offset value to move the curve without changing its shape and $C_i(\forall i \neq 0)$ controls the contribution of the Gaussian i with mean μ_i to the curve.

Since the contour delineates the luminal border, all the pixels inside this contour would correspond to lumen (foreground or class 1) while the pixels outside this contour would correspond to non-lumen (background or class 2). The class for each pixel in the image can be determined using the signed distance function: $g(x, C) = f(\theta, C) - r$, where the pixels with positive values have a higher probability of corresponding to lumen, and those with negative values to non-lumen. To deform the contour to find the luminal border, we want to take advantage of the membership of each pixel close to the contour of the two classes described above. Thus, we use a sigmoid function to define the probability $P_{in}(x)$ of each pixel x to belong to the class lumen as follows:

$$P_{in}(x) = \frac{1}{1 + e^{-\lambda(f(\theta,C)-r)}} .$$

Using this formulation the pixels far above the contour will have a probability close to one for belonging to lumen, while the pixels far below the contour will have probability close to zero. For the pixels near the contour, depending on the value of λ and their distance to the contour, the probability of these pixels belonging to lumen will be around 0.5.

Inspired by the Bayesian formulation for image segmentation proposed by Rivera *et al* [9], we propose the cost function:

$$U(C) = \sum_x P_{in}(x, C)^2 d_1(x) + P_{out}(x, C)^2 d_2(x) . \quad (2)$$

The functions d_1 and d_2 are defined as:

$$d_k(x) = -log(v_k(x, \phi_k)) \quad (3)$$

where $v_k(x, \phi_i)$ is the normalized likelihood of the pixel x to be generated by a model k with parameters ϕ_i. For our binary segmentation case:

$$P(x) = P_{in}(x, C) \quad (4)$$

$$P_{out}(x, C) = (1 - P(x, C)). \quad (5)$$

Using Eqs. (4) and (5), and since the square of a sigmoid function can be emulated with the same sigmoid function using different values of λ, we can rewrite (2) as:

$$U(C) = \sum_x P(x, C) d_1(x) + (1 - P(x, C)) d_2(x) , \quad (6)$$

As we will discuss later, for the minimization of this cost function we only need its first order derivatives. Due to the first order nature of our cost function, the analytical derivation of the gradient is very simple. Specifically, it is given by:

$$\nabla U(C) = \sum_x (d_1(x) - d_2(x)) \frac{\delta P(x, C)}{dC_n} ,$$

with

$$\frac{\delta P(x, C)}{dC_n} = \frac{\lambda \exp(-\lambda[f(\theta, C) - r])}{[1 + \exp(-\lambda[f(\theta, C) - r])]^2} \frac{\delta f(x, C)}{dC_n}$$

and

$$\frac{\delta f(x,C)}{dC_n} = \begin{cases} 2C_0 & \text{if } n = 0 \\ 2C_n[\sum_{i=1}^{N}(\exp(-\frac{1}{2\sigma^2}(\theta-\mu_i)^2)+ \\ \exp(-\frac{1}{2\sigma^2}(\theta+(w-1)-\mu_i)^2)+ \\ \exp(-\frac{1}{2\sigma^2}(\theta-(w-1)-\mu_i)^2))] & \text{otherwise} \end{cases}$$

We use the grey-level information (i.e., normalized histograms) to estimate the likelihood of each pixel to belong to the class lumen or the class non-lumen. To estimate these distributions, the user provides samples in the form of a binary map over the IVUS image (Fig. 3(a)). Then, the histograms of regions corresponding to foreground h_1 and background h_2 are computed using 50 bins and then normalized (Fig. 3(b)). We obtain the likelihoods v_{in} and v_{out} by using the value of the pixel grey-level $I(x)$ on the normalized histogram:

$$v_{in}(x) = \frac{h_{in}(I(x)) + \varepsilon}{h_1(I(x)) + h_2(I(x)) + 2\varepsilon},\ v_{out}(x) = 1 - v_{in} \tag{7}$$

where ε is a small constant. The likelihood for lumen (Fig. 4(a)) and non-lumen (Fig. 4(b)) are then used for computing the distances d_1 and d_2 by applying Eq. (3).

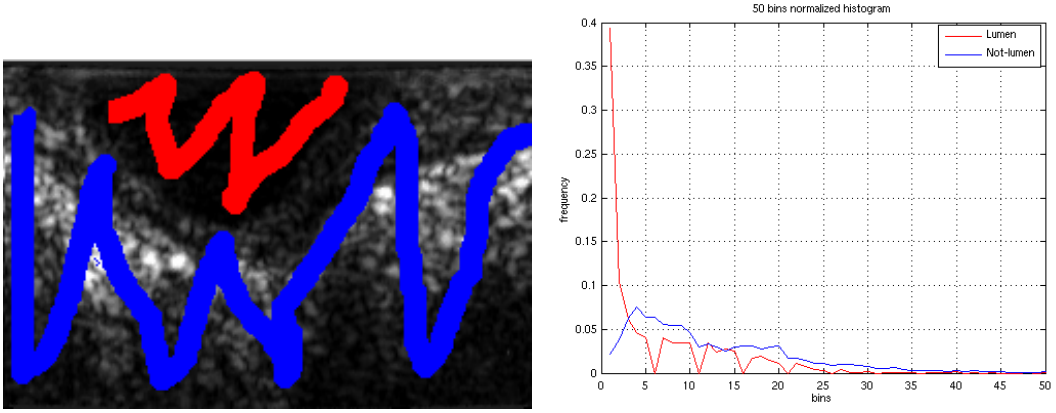

(a) (b)

Figure 3. User-provided information: (a) binary map with samples of the lumen and non-lumen; (b) normalized histogram of the intensities in the 2 classes.

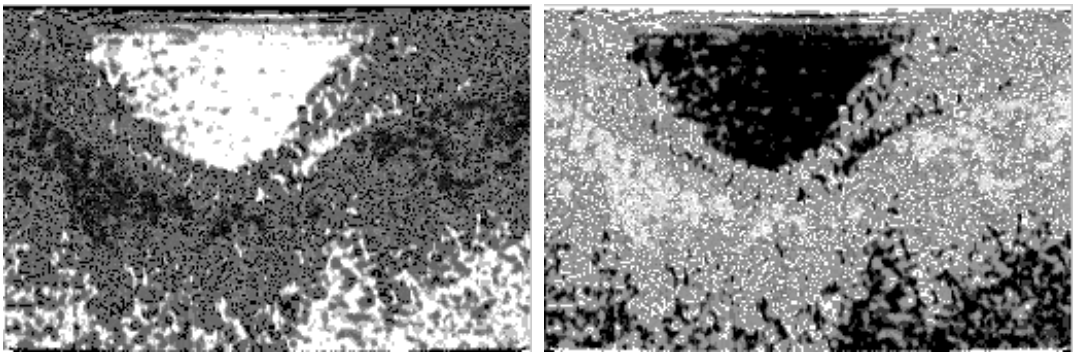

(a) (b)

Figure 4. Depiction of (a) the lumen likelihood and (b) the non-lumen likelihood.

3.1. Optimization method

A number of numerical methods exist to approximate the solution of this class of problems; one of the simplest ways is to use a steepest descent method. However, this approach could take a large number of iterations to converge to the solution.

Another possibility is to use the Quasi-Newton BFGS method [8]. This method uses second order information to find the optimal descent direction. However, since it is possible to find regions beyond the luminal border that have similar grey-level distribution to lumen, a large step in the optimization could lead to a different local minimal and hence an incorrect segmentation.

Thus, we propose an optimization method that uses a linear combination of the descent directions from steepest descent (p^G) and BFGS (p^{BFGS}) methods within a trust-region (similar to the dogleg method [8]). We will refer to this method as **G+BFGS optimization**.

In the BFGS method, the descent direction for each step is computed using $p_k^{BFGS} = -H_k \nabla f_k$, where H_k is an approximation to the Hessian that is updated on each iteration k by: $H_{k+1} = (I - \rho_k s_k y_k^T) H_k (I - \rho_k y_k s_k^T) + \rho_k s_k s_k^T$, with $\rho_k = \frac{1}{y_k^T s_k}$, $s_k = x_{k+1} - x_k$, and $y_k = \nabla f_{k+1} - \nabla f_k$. However, this method establishes a curvature condition that is given by: $s_k^T y_k > 0$. When $s_k^t y_k$ is greater than zero, the curvature of the function becomes more positive as the descent approaches a minimal. If $s_k^t y_k < 0$, the curvature condition is not satisfied and a better descent direction is the negative gradient (i.e., steepest descent direction). Additionally, we can note that for small values of the product $s_k^t y_k$, the computation of the update formula for the Hessian (or its inverse) is undefined.

By design, the more positive the value of ρ, the better the step direction will be. Thus, the contribution of the BFGS descent direction p_k^{BFGS} will be small when ρ is small (preferring steepest descent direction p_k^G). On the other hand, if the value of ρ is more positive, we want to take the BFGS descent direction p_k^{BFGS}. Based on this analysis, we propose to compute the descent direction as a linear combination of both descent directions: $p_{k+1}^{G+BFGS} = -[(\psi(\rho_k)) H_k \nabla f_k) + ((1 - \psi(\rho_k)) \nabla f_k)]$, where the function that controls the contribution of each descent direction $\psi(\rho)$ is defined as:

$$\psi(\rho) = \begin{cases} 0 & \text{if } \rho < 0 \\ \frac{\rho^2}{K + \rho^2} & \text{otherwise} \end{cases} \tag{8}$$

with the constant K experimentally determined to be $K = 1 \times 10^{-4}$.

Although the problem with the curvature condition is solved using this linear combination, when using BFGS, if in some step the value of the inner product of $y_k^T s_k$ is very small (but positive) then the value of ρ becomes big and therefore H_{k+1} becomes very big (even when the calculated step size α satisfies the Wolfe conditions [8]), making the step too big. This is undesirable because a big step could lead to an incorrect segmentation moving the lumen contour to a region with grey-level profile similar to that of the lumen. To solve this problem, we propose to restrict our proposed descent direction magnitude within a trust region controlled by a fixed parameter T. Thus, after obtaining p_k^{G+BFGS}, the descent direction is normalized:

$$\hat{p}_k^{G+BFGS} = \frac{p_k^{G+BFGS}}{\| p_k^{G+BFGS} \|},$$

and the final descent direction is the normalized descent direction $\hat{p}_k^{G+BFGS}$ scaled by the parameter of thrust region T: $P_k^{G+BFGS} = T \hat{p}_k^{G+BFGS}$

3.2. Multi-Scale segmentation

The number of Gaussians N and the value of σ used to represent the lumen contour depends on the width w of the IVUS image to be segmented. However, a large number of Gaussians will imply a longer computation. To accelerate the convergence of our segmentation method, we use a multi-resolution approach: At first step ($i = 0$) a small number of Gaussians N_i is used (3 to 5). Once the optimization converges more Gaussians are added and the optimization is repeated again using as initialization the contour of the previous scale. This process is repeated until the maximum number of Gaussians is reached. In addition, the value of σ is reduced as the number of Gaussians is incremented.

To get the coefficients C_{i+1} for the lumen curve $y_i(\theta)$ (Fig. 5(a)) from the previous iteration, it is necessary to adjust the last contour to the function with the new number of Gaussians N_{i+1} (Fig. 5(b)). Thus, we use the least squares method for computing the starting point for the new segmentation: $C_{i+1} = \min_C \ \frac{1}{2}[f(\theta, C) - y(\theta)]^2$, s.t. $C_i \geq 0$.

3.3. IVUS images segmentation algorithm

To initiate segmentation, we need to assign the following parameters:
The **sigmoid** λ is related to the uncertainty around the lumen-contour; this parameter controls how much the contour can be deformed on a given iteration. The typical value (experimentally selected) for this parameter is $\lambda \epsilon [.5, 1]$.

Algorithm 1 G+BFGS optimization

Require: Initial point x_0, thrust region value T, and a tolerance ε.

Initialize $H_0 = I$
$p_k^{G+BFGS} = -\nabla f(x_0)$
$k = 0$
while $\|\nabla f(x_k)\| > \varepsilon$ **do**
  $\hat{p}_k^{G+BFGS} = \frac{p_k^{G+BFGS}}{\|p_k^{G+BFGS}\|}$
  $P_k^{G+BFGS} = T\hat{p}_k^{G+BFGS}$
  Compute the step size α_k to satisfy the Wolfe conditions
  $x_{k+1} = x_k + \alpha P_k^{G+BFGS}$
  $s_k = x_{k+1} - x_k$
  $y_k = \nabla f(x_k + 1) - \nabla f(x_k)$
  $\rho_k = \frac{1}{y_k^T s_k}$
  $H_{k+1} = (I - \rho_k s_k y_k^T) H_k (I - \rho_k y_k s_k^T) + \rho_k s_k s_k^T$
  $p_{k+1}^{G+BFGS} = -[\psi(\rho_k) H_k \nabla f_k + (1 - \psi(\rho_k)) \nabla f_k]$
  $k = k + 1$
end while

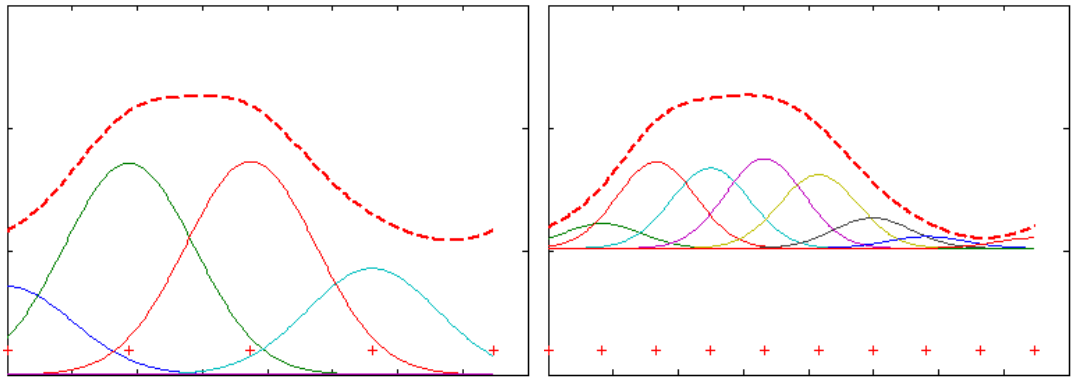

(a) (b)

Figure 5. Adjustment of the lumen contour: (a) lumen contour modeled using 5 Gaussians) and (b) contour adjusted to be modeled using 10 Gaussians. The + symbol indicates the Gaussian means and the dashed line the lumen contour.

The **initial point** C_{init}: Since our problem has a minimum on $C = 0$, the initial point C_{init} must be different from zero to avoid the trivial solution. We have found that it is convenient to set the offset coefficient to be at least the square of one quarter of the image height $C_0[0] = \sqrt{h/4}$ and the rest of the coefficients to be half of the offset.
The **number of Gaussians** for each of the multi-scale steps depends on the width w of the IVUS image; ideally we would like the Gaussians to cover all the image width. These values form a vector $NG = \{N_0, N_1, ..., N_{max}\}$ where max is the maximum number of Gaussians allowed.
The **mean** of each Gaussian: This parameter is chosen such that the Gaussians are uniformly distributed into the image width.
The value of **standard deviation** σ for each one of the multi-scale steps: in the first steps coverage rather than accuracy is of importance. In the last step, however, the value should be higher to increase accuracy. These values form the vector $\Sigma = \{\sigma_0, \sigma_1, ..., \sigma_{max}\}$ with the values σ for each step.

For a typical 20MHz IVUS image (Fig. 6(a)), once the histograms and likelihoods are computed from the user-provided map, the segmentation begins with the contour corresponding to the initial point C_{init}. In Fig. 7, we observe that in the first iterations of the first multi-scale step, the lumen-contour quickly deforms until it reaches a rough approximation of the luminal border shape. When this step converges, additional Gaussians with a different standard deviation are added to the contour in order to get a better approximation. In Fig. 8(a) we can observe that at the end of step 2 the lumen-contour is starting to look similar to the lumen boundary. On step three, additional Gaussians are added and at the end of this step the lumen-contour is very close to solution (Fig. 8(b)). On the last step, the maximum number of Gaussians is used and the

Algorithm 2 Probabilistic segmentation for IVUS images

Require: IVUS image I on polar representation, an array with the values of the number of Gaussians to be used $NG = \{N_0, N_1, ..., N_{max}\}$, an array with the values of the standard deviations $\Sigma = \{\sigma_0, \sigma_1, ..., \sigma_{max}\}$ for each step, the starting point C_{init} and h_1 and h_2 computed from the map of the luminal area.

1: Compute the normalized histograms h_1 and h_2 form the map.
2: Compute the likelihoods v_{in} and v_{out} using (7).
3: Compute the distances d_1 and d_2 using (3)
4: $i = 0$
5: **while** $i \leq max$ **do**
6: Find the lumen contour y_i by solving (6) using the G+BFGS method of algorithm 1.
7: Compute C_{i+1} using the least squares method with y_i
8: i=i+1
9: **end while**

resulting lumen-contour is more detailed when compared to the one obtained at the previous step (Fig. 8(c)). Fig. 6(b) depicts the segmentation of the image in Fig. 6(a).

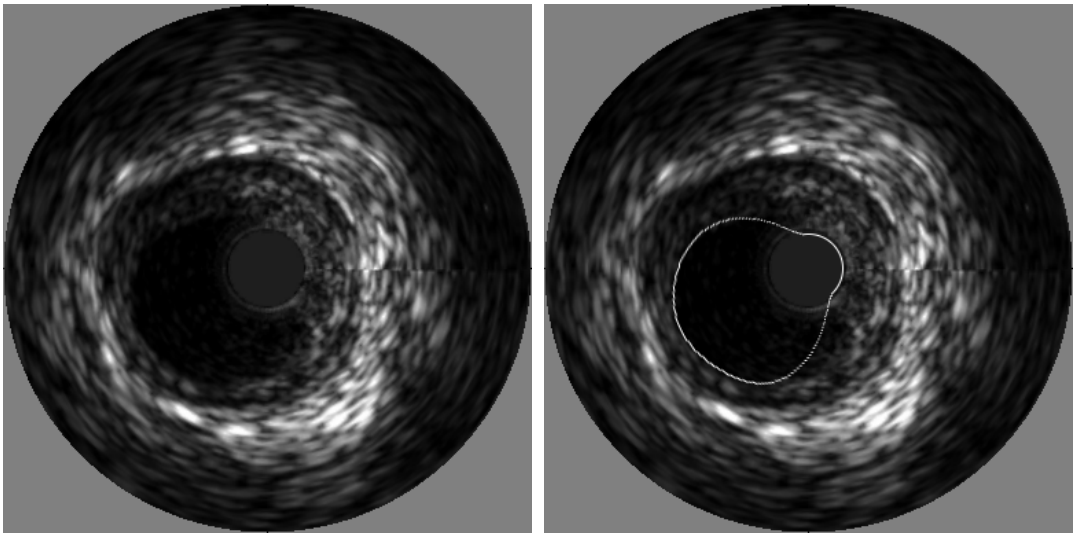

(a) (b)

Figure 6. A typical 20 MHz IVUS image. (a) image to segment, (b) segmentation result.

3.4. Video sequence segmentation

Segmentation of a complete video sequence requires initialization of the first frame as indicated earlier. Based on the fact that two consecutive IVUS frames have similar luminal -level distribution, we use the histogram from the previously segmented frame to compute the likelihoods for the current frame. Similarly, the lumen-contour of the previously segmented frame is used as initial contour for the current frame. For reasons of computational efficiency, only the first frame is segmented starting with a small number of Gaussians; for the segmentation of the consecutive frames we start with the maximum number of Gaussians permitted. Furthermore, it is well known that as the number of samples is increased, the grey-level values class distribution is better estimated by the histogram technique and provides more accurate *a priori* information. We take advantage of this fact by accumulating the histograms of the previously segmented frames from the video sequence and using them on the consecutive frames. This procedure can be seen as a reinforcement learning process. Algorithm 3 presents our approach for semi-automatic segmentation of IVUS video sequences based on our proposed probabilistic segmentation method.

Fig. 9 depicts the segmentation of four consecutive frames.

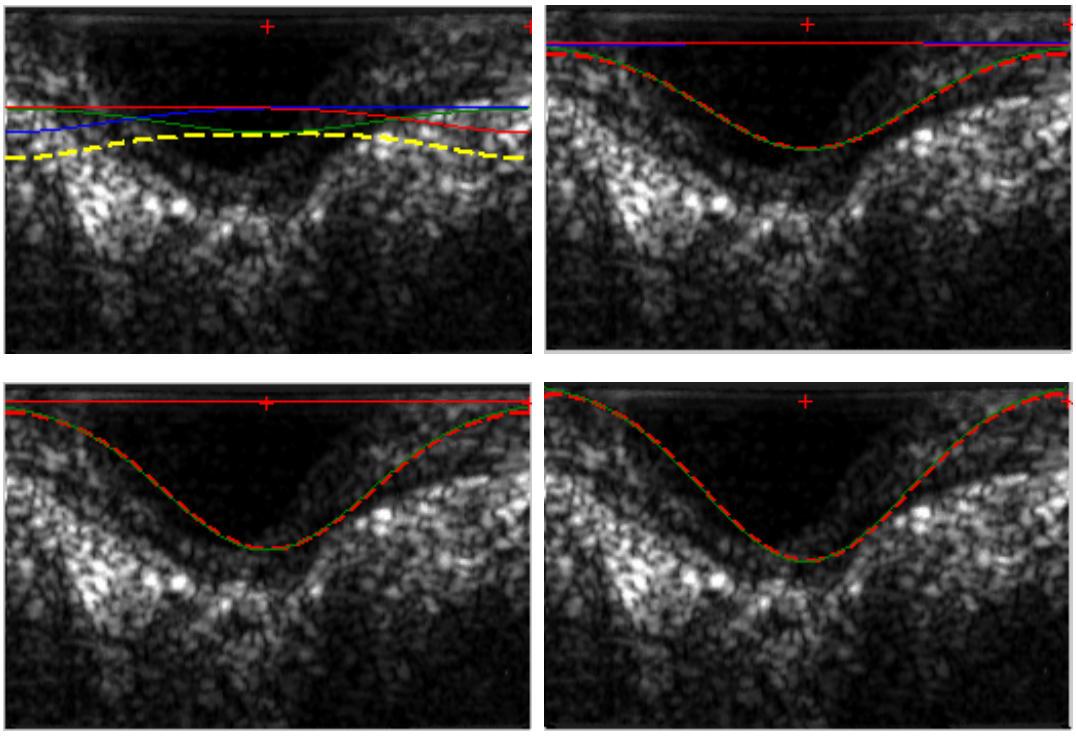

Figure 7. Depiction of the deformation of the lumen contour during step 1 the multi-scale method. (a) Initial contour, and after (b,c,d) 5, 15, and 40 iterations, respectively.

Algorithm 3 Probabilistic segmentation for IVUS video sequences

Require: An array with the values of the number of Gaussians to be used $NG = \{N_0, N_1, ..., N_{max}\}$, an array with the values of the standard deviations $\Sigma = \{\sigma_0, \sigma_1, ..., \sigma_{max}\}$ for each step, starting point C_0 and h_1 and h_2 computed from the map of the luminal area of the first frame F_0.

1: $H_1 = h_1$, $H_2 = h_2$.
2: $i = 0$
3: **while** $i <=$ Number of frames **do**
4: Segment frame F_i with algorithm 2 using H_1 and H_2 as the histograms and C_i for initialization.
5: Compute h_1 and h_2 from the segmented frame F_i
6: $H_1 = H_1 + h_1$, $H_2 = H_2 + h_2$
7: Obtain $C_i + 1$ using the least squares method with the segmentation result.
8: i=i+1
9: **end while**

4. Results

We evaluated our method by computing the three measures of accuracy recommended by Udupa *et al* [11]. Specifically, we computed the false negatives (FN), false positives (FP), true negatives (TN), and true positives (TP) by computing the number of pixels that were classified as background and lumen. For a set of 100 20MHz IVUS images, the mean accuracy was $98.28\% \pm 0.49\%$, the mean true negative rate was $99.43\% \pm 0.29\%$ and the mean true positive rate was $95.57\% \pm 1.69\%$.

The agreement between the areas of the lumen was analyzed using the linear regression analysis and Bland-Altman [1] plots. The inter-observer and automatic (A) mean biases and variabilities for two manual segmentations (MS1 and MS2) for lumen are: the bias of the differences between A and MS1 (A,MS1) was 369.70 ± 336.56; for (A,MS2) the bias was 453.57 ± 304.89 and for (MS1,MS2) was 83.87 ± 343.61. Fig. 10 depicts the results of this analysis.

Results on IVUS images with artifacts: The principal problem of previous segmenting methods is related to how the artifacts on the IVUS images are handled. Fig. 11 depicts the segmentation result on an image with a shadow artifact

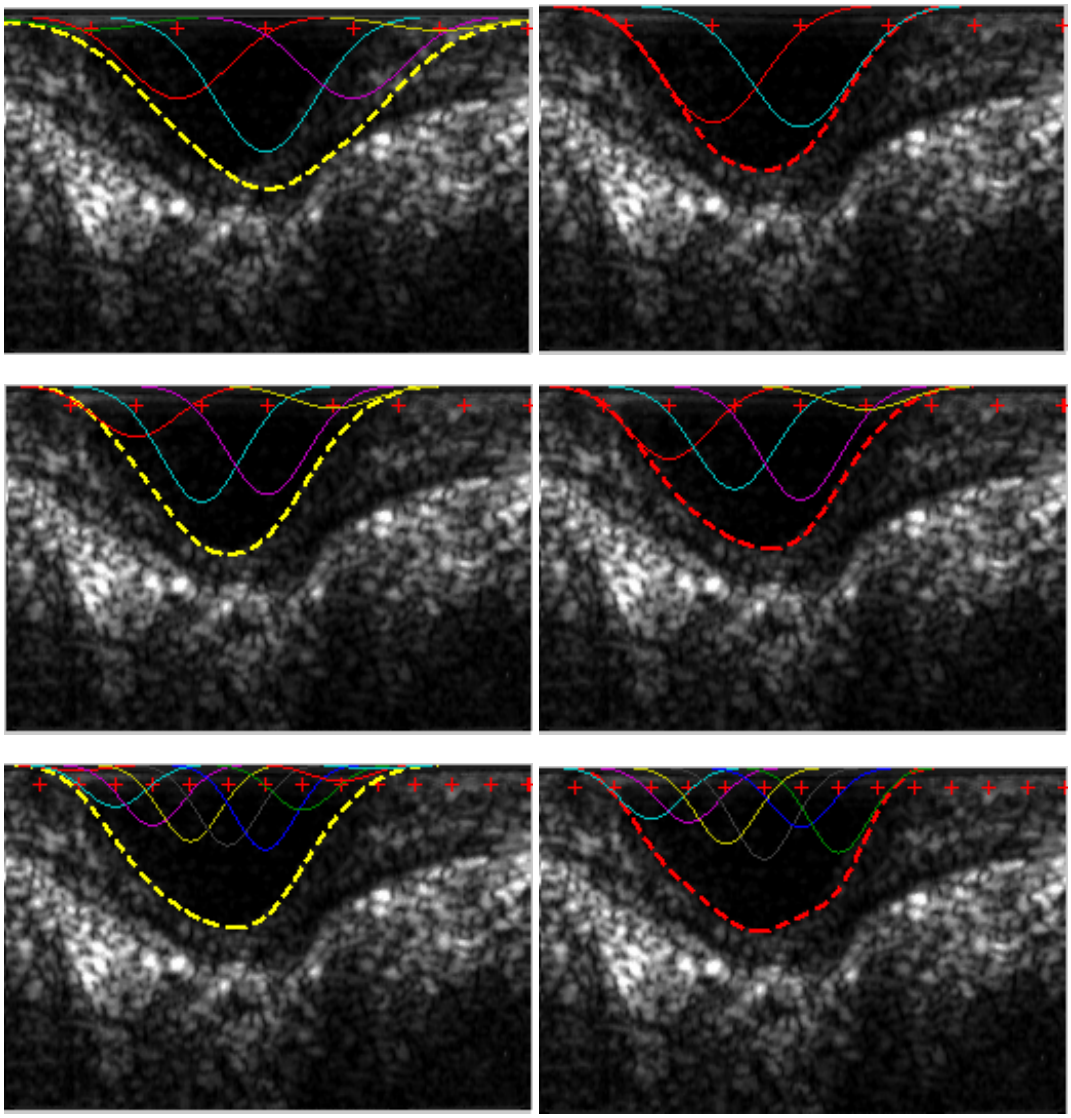

Figure 8. Depiction of the deformation of the lumen contour during steps 2, 3 and 4 (a,b,c) respectively of the multi-scale method. *(left, right) initial and final contours respectively.*

due to calcified plaque. Although this shadow could be mistakenly interpreted as lumen since it has grey-level intensities similar to the lumen region, we can observe that our segmentation method was able to find the luminal border correctly. Normally the ringdown artifacts are removed by cropping the region that presents this artifact or simply replacing it with some uniform color; however sometimes this artifact is not removed. Since guidewire artifacts are more difficult to remove, they are commonly found on IVUS images. Because this artifact shows a bright profile, it can easily be confounded with plaque or other tissue and lead to an incorrect segmentation. Fig. 12 depicts the segmentation result on an IVUS image with three artifacts: a ringdown artifact, a small guidewire artifact, and a shadow artifact. As we can see, none of these artifacts affected the performance of the segmentation.

Fig. 13 depicts the segmentation result on an IVUS image with two artifacts: shadow in all the areas beyond the plaque due to calcified plaque, and a larger guidewire than the one on the IVUS image in Fig. 12. Our method was capable of segmenting the image despite the shadow and the guidewire artifact.

Side branches are identified as the opening formed when the vessel being imaged bifurcates. This is visualized as an area of dark intensity extending from the lumen in the near field towards the far field; this represents a challenge for any active-contour based segmentation method because the segmenting contour could advance through this shadow and lead to an incorrect segmentation of the luminal border. Fig. 14 depicts the segmentation result on an IVUS image of a relative

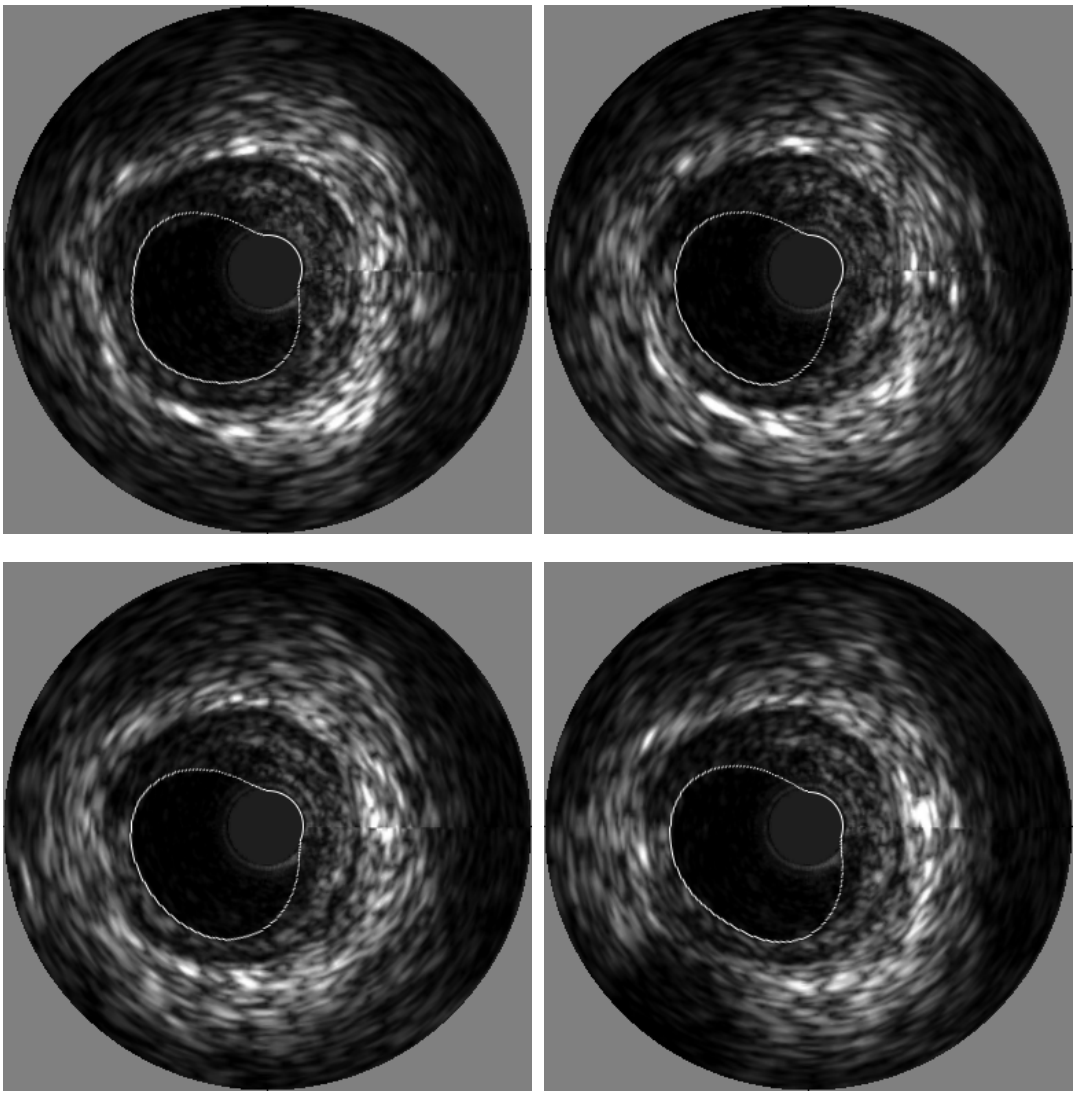

Figure 9. Segmentation of 4 consecutive frames

healthy vessel (i.e., only a small plaque is present) with a side branch. In our method, the smoothness of our segmenting contour resolves the problem with branches. However, if we change the smoothness to achieve a better detail, the contour will tend to attempt to segment the side branch as lumen and we will obtain incorrect segmentation.

5. Conclusion

We have presented a probabilistic semi-automatic segmentation method for lumen segmentation of IVUS images that is robust to artifacts and that does not require prior training. Our proposed G+BFGS optimization has shown itself to be an ideal method for this kind of problem because it is faster than the steepest descent optimization by itself and at the same time it can be controlled to avoid big steps that lead to an incorrect segmentation. In addition, our contour parameterization makes possible the multi-scale segmentation that considerably increases the segmentation speed on fixed images and video sequences, allowing us to get more accurate segmenting-contours on the last step as well.

In our experiments, this method has shown a good performance on segmenting fixed 20MHz IVUS images and video sequences. However, on higher-frequency IVUS images (i.e., 30-40 MHz) the speckle noise will be higher making it difficult to segment with our method since we use only grey-level histograms to compute the likelihoods. To solve this problem, we believe that by incorporating texture features in our *a priori* information [3], we will have better likelihoods that would lead

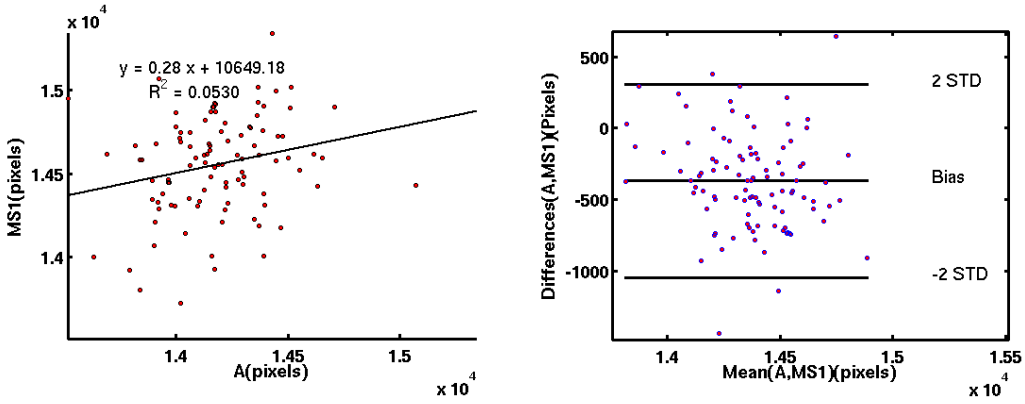

(a)

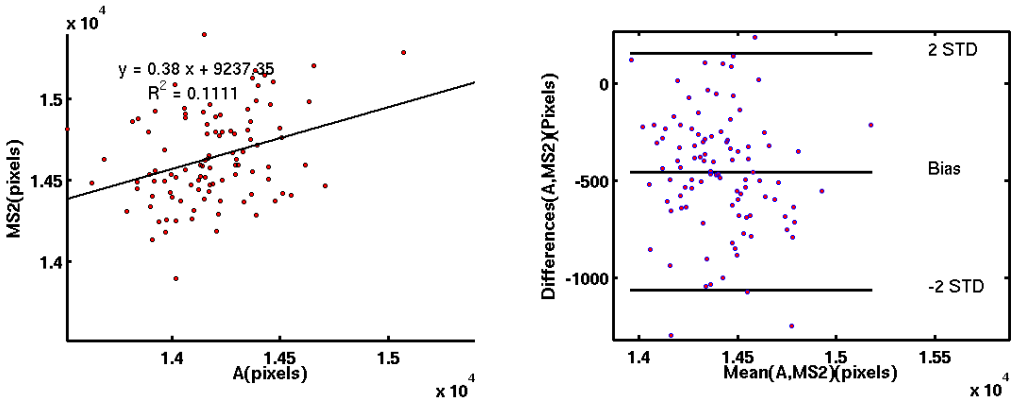

(b)

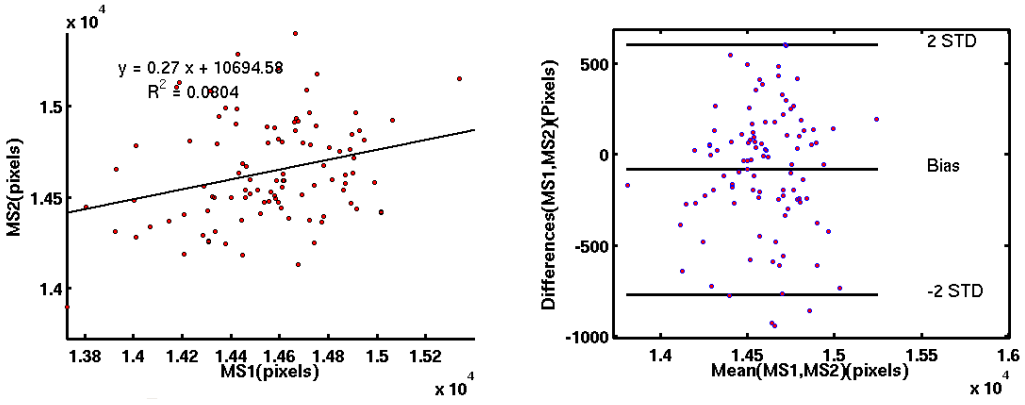

(c)

Figure 10. Bland-Altman plots for lumen segmentation: (a) Automatic vs. Manual segmentation 1, (b) Automatic vs. Manual segmentation 2, (c) Manual segmentation 1 vs. Manual segmentation 2.

to a successful segmentation on those modalities.

Media/adventitia border segmentation is still a problem to be solved by our method. However, since the media is observed as a thin black line and the adventitia tissue appears very bright because of its echogenic characteristics [12], we believe that this same formulation will work to segment the media/adventita contour by combining pixel intensities with image-gradient information [6] on the *a priori* information (i.e., likelihoods) with some minor modifications to our segmentation method.

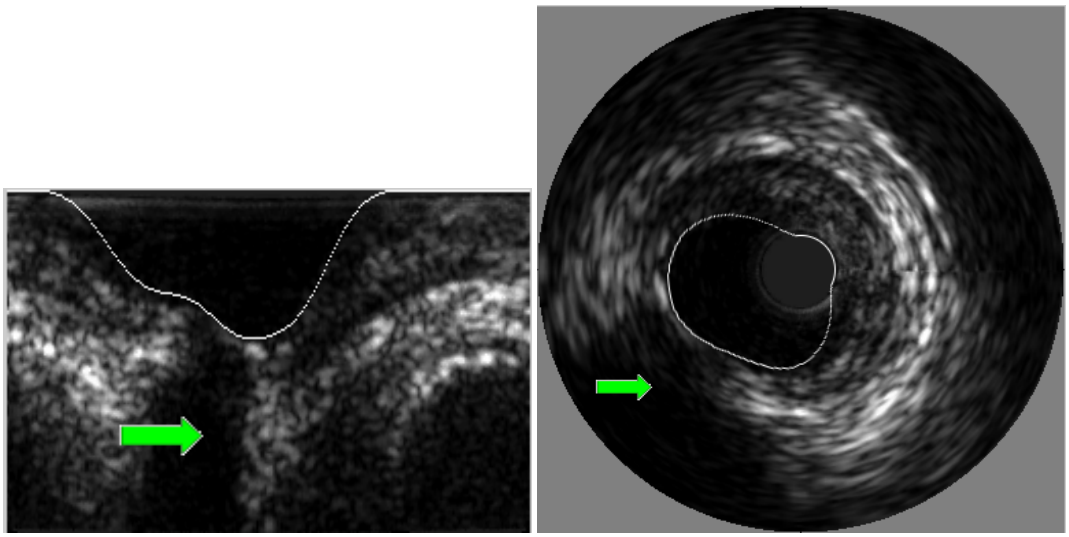

Figure 11. Segmentation example of IVUS image with shadow artifact: segmentation result. *The arrow indicates the shadow artifact due a calcified plaque.*

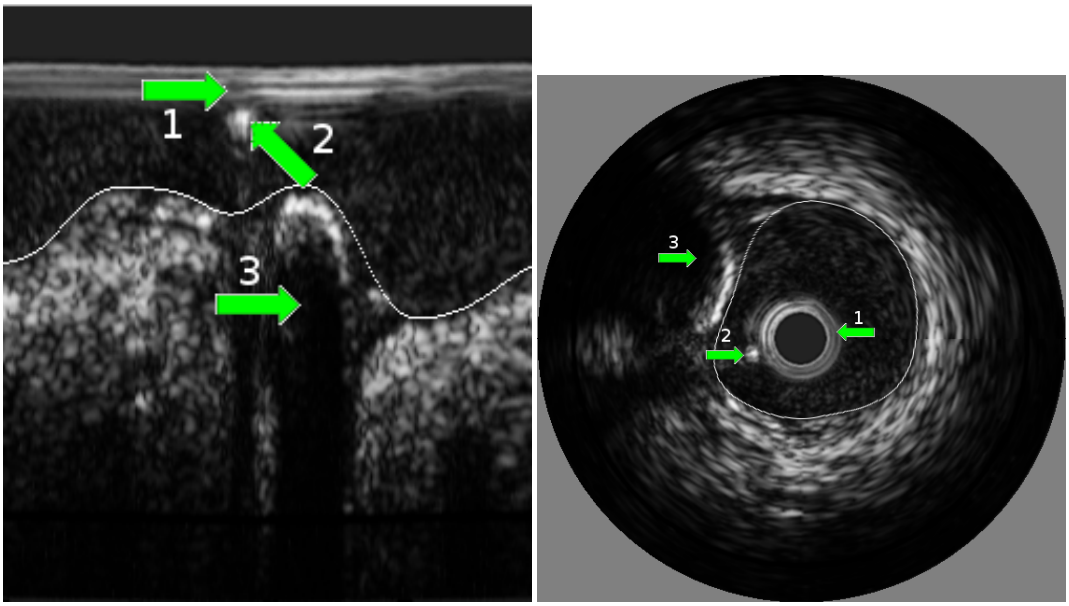

Figure 12. Segmentation example of IVUS image with various artifacts: segmentation result. *The arrows indicate the artifacts: (1) rigndown artifact; (2) guidewire artifact; (3) shadow artifact.*

References

[1] J. Bland and D. G. Altman. Statistical methods for assessing agreement between two methods of clinical measurement. *Lancet*, 1:307–310, 1986. 8

[2] E. Brusseau and C. L. de Korte. Fully automatic luminal contour segmentation in intracoronary ultrasound imaging - a statistical approach. *IEEE Trans. on Med. Imag.*, 2004. 2

[3] E. dos Santos Filho, M. Yoshizawa, A. Tanaka, and Y. Saijo. A study on intravascular ultrasound image processing. *Record of Electrical and Communication Engineering Cconversazione Tohoku University*, 74(2):30–33, 2006. 10

[4] C. Haas, H. Ermert, S. Holt, P. Grewe, A. Machraoui, and J. Barmeyer. Segmentation of 3d intravascular ultrasonic images based on a random field model. *Ultrasound Med. Biol.*, 26(2):297–306, 2000. 1

[5] J. D. Klingensmith, R. Shekhar, and D. G. Vince. Evaluation of three-dimensional segmentation algorithms for the identification of luminal and medial-adventitial borders in intravascular ultrasound images. *IEEE Trans. Med. Imag*, 19(10):996–110, Oct 2000. 1

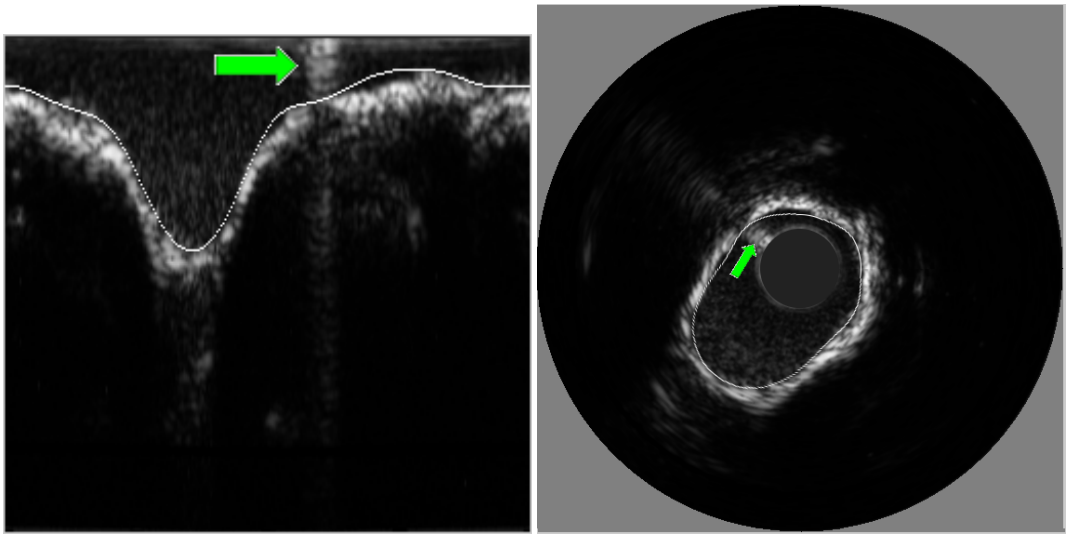

Figure 13. Segmentation example of IVUS image with guidewire artifact: segmentation result. *The arrow indicates the guidewire artifact.*

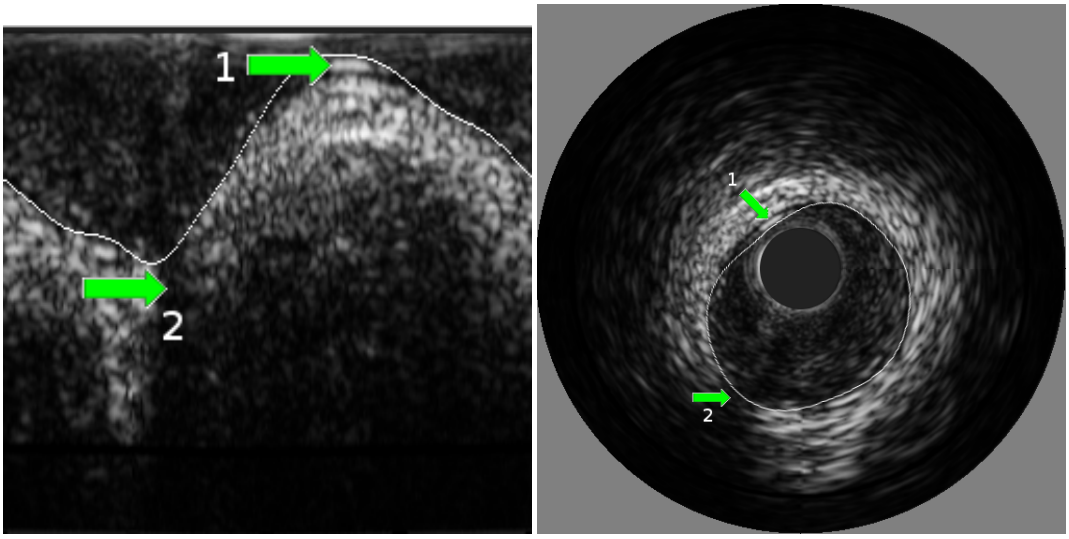

Figure 14. Segmentation example of IVUS image with side branch: segmentation result. *Arrow (1) indicates the small plaque and arrow (2) the side branch.*

[6] G. Kovalski, R. Beyar, R. Shofti, and H. Azhari. Three-dimensional automatic quantitative analysis of intravascular ultrasound images. *Ultrasound Med. Biol*, 26(4):527–537, 2000. 1, 11

[7] A. Mojsilovic, M. Popovic, N. Amodaj, R. Babic, and M. Ostojic. Automatic segmentation of intravascular ultrasound images: a texture-based approach. *Ann. Biomed. Eng.*, 25(6):1059–1071, 1997. 1

[8] J. Nocedal and S. J. Wright. *Numerical Optimization*. Springer, 1999. 5

[9] M. Rivera, O. Ocegueda, and J. L. Marroquin. Entropy-controlled quadratic Markov measure field models for efficient image segmentation. *IEEE Trans. Image Processing*, 8(12):3047–3057, Dec. 2007. 1, 3

[10] M. Sonka and X. Zhang. Segmentation of intravascular ultrasound images: A knowledge-based approach. *IEEE Trans. on Medical Imaging*, 14:719–732, 1995. 2

[11] J. Udupa, Y. Jin, C. Imielinska, A. Laine, W. Shen, and S. Heymsfield. Segmentation and evaluation of adipose tissue from whole body MRI scans. In *Proc. 6th International Conference on Medical Image Computing and Computer-Assisted Intervention, Montreal, Canada, November 15-18*, pages 635–642, 2003. 8

[12] G. Unal, S. Bucher, S. Carlier, G. Slabaugh, T. Fang, and K. Tanaka. Shape-driven segmentation of intravascular ultrasound images. In *Proc. International Workshop on Computer Vision for Intravascular Imaging (CVII), MICCAI, Copenhagen, Denmark.*, 2006. 2, 11

[13] C. von Birgelen, C. D. Mario, W. Li, J. C. H. Schuurbiers, C. J. Slager, P. J. de Feyter, P. W. Serruys, and J. R. T. C. Roelandt. Morphometric analysis in three-dimensional intracoronary ultrasound: an in vitro and in vivo study using a novel system for the contour detection of lumen and plaque. *Am. Heart J.*, 132(2):516–527, 1996. 1

[14] X. Zhang, C. R. McKay, and M. Sonka. Tissue characterization in intravascular ultrasound images. *IEEE Trans. Med. Imag*, 17(6):889–899, Dec 1998. 1